ceramics

MDPI

Article

Hydrothermal Synthesis Optimization of High-Aspect Ratio α-Al_2O Microfibers for Thermally Conductive Soft Composites

Omar Zahhaf [1], Giulia D'Ambrogio [1], François Grasland [2], Guilhem Rival [1], Minh-Quyen Le [1], Pierre-Jean Cottinet [1] and Jean-Fabien Capsal [1,*]

[1] LGEF, INSA-Lyon, UR682, University Lyon, 69621 Villeurbanne, France; guilhem.rival@insa-lyon.fr (G.R.); minh-quyen.le@insa-lyon.fr (M.-Q.L.); pierre-jean.cottinet@insa-lyon.fr (P.-J.C.)
[2] GETELEC, 78530 Buc, France; francois.grasland@getelec.net
* Correspondence: jean-fabien.capsal@insa-lyon.fr

Abstract

This work presents a comprehensive study on the synthesis and application of Al_2O_3 fibers derived from an ammonium aluminum carbonate hydroxide (AACH) precursor. Through a hydrothermal route, the influence of critical synthesis parameters, including aluminum nitrate and urea concentrations, reaction temperature and time, and stirring conditions, on fiber morphology and aspect ratio was systematically investigated. The as-synthesized AACH fibers were subsequently converted into thermodynamically stable α-alumina fibers via controlled annealing. These high-aspect ratio alumina fibers were incorporated into polydimethylsiloxane (PDMS) to produce electrically insulating, thermally conductive composites. The thermal performance of fiber-filled composites was benchmarked against that of particle-filled counterparts, with the former exhibiting significantly enhanced thermal conductivity. Furthermore, the dielectrophoretic alignment of alumina fibers led to an additional increase in thermal conductivity, underlining the importance of high-aspect ratio fillers. This study uniquely combines the controlled synthesis of alumina fibers with their incorporation and alignment in a polymer matrix, presenting a novel and effective approach for engineering anisotropic, thermally conductive, and electrically insulating composite materials. Dielectrophoretic alignment of α-Al_2O_3 fibers synthesized through optimized hydrothermal conditions and incorporated into PDMS composites deliver over 95 % higher thermal conductivity than spherical fillers.

Keywords: α-Al_2O_3 microfibers; hydrothermal synthesis optimization; morphology and aspect ratio control; thermally conductive composites

Academic Editor: Frank Kern

Received: 29 July 2025
Revised: 23 September 2025
Accepted: 6 October 2025
Published: 9 October 2025

Citation: Zahhaf, O.; D'Ambrogio, G.; Grasland, F.; Rival, G.; Le, M.-Q.; Cottinet, P.-J.; Capsal, J.-F. Hydrothermal Synthesis Optimization of High-Aspect Ratio α-Al_2O Microfibers for Thermally Conductive Soft Composites. *Ceramics* **2025**, *8*, 127. https://doi.org/10.3390/ceramics8040127

1. Introduction

The development of soft, thermally conductive, and electrically insulating materials is a scientific challenge [1–3] that needs to be unraveled for industrial applications such as integrated circuits, power electronics, computer chips, and other electronic component packaging [4]. A classical route to obtaining thermally conductive soft materials involves the hybridization of polymers with highly thermally conductive inorganic particles [5–7]. In most cases, inorganic particles present a low aspect ratio, requiring a high filler volume content [8,9]. Consequently, these materials become dense, stiff, and brittle. In recent years, numerous studies have explored the development of tailored synthesis routes to produce architectured particles, such as nanowires and nano-cubes, in order to address these issues [10–12].

In this context, percolation [13] and connectivity theories [14] have demonstrated that the use of high-aspect ratio particles allows for the reduction in the inorganic phase content in hybrid composites [15,16]. For example, these high-aspect ratio particles have found numerous applications in the fields of electrically [17] and thermally conductive materials [18,19], as well as piezoelectric and pyroelectric materials [20–22]. Using high-aspect ratio particles in thermally conductive composites reduces interparticle thermal resistance, thus increasing the heat flux exchange across the material. As a bridge between electrically conductive and thermally conductive materials, one way to reduce the filler content is through percolation theory. In this theory, the filler aspect ratio is one of the most important parameters, driving the optimal volume content to achieve the desired applicative properties [13]. The filler aspect ratio represents a key element in determining the overall performance of composite materials, particularly through its influence on the composite's structural connectivity [14,15], as it significantly affects the filler size to inter-filler ratio, interfacial interactions, and heat transfer efficiency within the composite structure.

α-Al_2O_3 is one of the most promising thermally conductive ceramic materials due to its combination of high thermal conductivity, large bandgap (5.97 eV), and low cost [23,24], making it an ideal candidate for the development of electrically insulating thermal interface materials. While various synthesis routes for α-Al_2O_3 fibers have been reported [25–27], hydrothermal synthesis offers a scalable and controllable method for producing fibers with tunable morphology [28,29]. In this work, we investigate the hydrothermal synthesis of ammonium aluminum carbonate hydroxide (AACH) fibers as a precursor to α-Al_2O_3 fibers, with a focus on controlling aspect ratio through process parameters such as temperature, reaction time, stirring, and precursor concentration. The resulting fibers are thermally annealed to achieve the α-phase and then incorporated into PDMS-based composites. Finally, we compare fiber-filled and particle-filled composites, both in unstructured and dielectrophoretically structured configurations, to evaluate the influence of filler morphology and alignment on thermal conductivity. This study aims to establish a direct link between synthesis-controlled fiber geometry and the thermal properties of structured polymer composites. This work advances current understanding in three distinct directions. It first explores the joint optimization of hydrothermal synthesis parameters—such as precursor concentration, agitation, reaction time, and temperature—an approach seldom addressed in a systematic manner. It then reveals the formation of a transient boehmite (AlOOH) phase under hydrothermal treatment at 160 °C for 24 h, a phenomenon only rarely noted in the literature. Finally, it demonstrates that incorporating α-Al_2O_3 fibers, oriented by dielectrophoresis, into PDMS matrices leads to a marked rise in thermal conductivity, with values exceeding those of spherical fillers by more than 95%. These outcomes highlight both the originality of the methodology and its potential technological impact.

2. Materials and Methods

All chemical products used were of analytical grade and did not require any additional purification. A standard synthesis procedure involves dissolving 20 mmol of $Al(NO_3)_3{\cdot}9H_2O$, 0.36 mol of urea and 0.1 mmol of polyethylene glycol (6000 g/mol) in 65 mL of deionized water [25,30]. Although polyethylene glycol does not actively participate in the chemical reactions, it plays the important role of being a template for the growth of ammonium aluminum carbonate hydroxide (AACH) fibers according to the surfactant-induced fiber formation (SIFF) mechanism [25]. The prepared solution is then magnetically stirred for 1 h at 400 rpm. 40 mL of the obtained solution is poured into a 100 mL PTFE container and secured inside an autoclave. The autoclave is then heated to 140 °C at 3 °C/min and maintained at 140 °C for 24 h while the solution is magnetically stirred at 250 rpm. Subsequently, the autoclave is cooled down naturally to room

temperature and the product of the reaction is collected and diluted in 500 mL of distilled water then stirred for 12 h at 400 rpm. The obtained AACH fibers are then washed and filtered twice in distilled water and once in ethanol to remove any remaining impurities. Finally, the fibers are dried at 80 °C for 4 h. It is important to note that the parameters of hydrothermal synthesis, such as temperature, time and reactant concentrations, play an important role in the resulting fibers [28]. Such parameters were investigated in the current study.

γ-Al_2O_3 fibers are obtained by annealing the AACH fibers at 900 °C for 4 h with a heating rate of 1 °C/min. Subsequently, α-Al_2O_3 fibers are obtained by annealing the γ-Al_2O_3 fibers at 1200 °C for 6 h with a heating rate of 1 °C/min. Alternatively, α-Al_2O_3 can be obtained directly from the fibers by annealing them at 1200 °C for 8 h at a heating rate of 1 °C/min [30]. Figure 1 shows a schematic representation of the synthesis and annealing process.

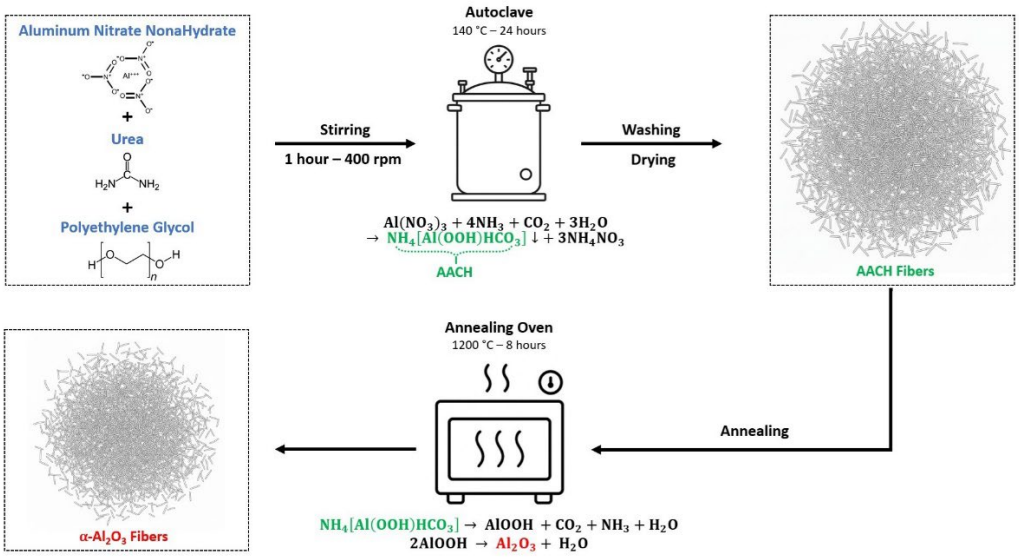

Figure 1. Schematic representation of the synthesis and annealing process.

For each condition, three independent syntheses were carried out. The analysis of fiber length revealed a variance of ±15%, while the yield exhibited a variance of ±10%. These values confirm the reproducibility and robustness of the synthesis procedure.

For the sake of completeness, the resulting α-Al_2O_3 fibers were used to fabricate both structured and unstructured PDMS-based. PDMS-Al_2O_3 composites were prepared by dispersing the required amount of alumina fillers into Sylgard 184 base (part A, Dow Corning, Midland, MI, USA). The mixture was mechanically stirred for 5 min and sonicated for 5 min (UP400S, Hielscher Ultrasonics, Teltow, Germany) to prevent filler aggregation. Afterward, the curing agent (part B) was added and the blend was stirred for an additional 5 min, followed by vacuum degassing at room temperature for 5 min to eliminate trapped air bubbles. The homogeneous blend was poured into the lower part of the molds and degassed again before sealing with the upper part. To ensure uniform sample thickness, both molds were subjected to identical compression. For the 1–3 structured composite, the mold was exposed to a high-voltage AC electric field (Trek 20/20C amplifier, Advanced Energy, Denver, CO, USA and 33210A generator, Keysight, Santa Rosa, CA, USA) for 1 h at room temperature, while voltage and current were monitored (DSOX3054A oscilloscope, Keysight, Santa Rosa, CA, USA). The temperature was then raised to 120 °C (5–10 °C/min) under the applied field, and curing was performed at 120 °C for 1 h. For the 0–3 unstructured composite, curing was carried out directly at 120 °C for 1 h without applying the electric field. After

curing, all samples were cooled naturally to room temperature. For further details on the development of PDMS-based structured composites shaped by dielectrophoresis, the reader is referred to our previous publications arising from the work of our laboratory [22].

To evaluate the morphological and structural characteristics of the synthesized fibers, scanning electron microscopy (SEM) and X-ray diffraction (XRD) were performed at various stages of the process. SEM analyses were performed on a FlexSEM 1000 II manufactured by Hitachi (Tokyo, Japan) while XRD analyses were performed on a X'Pert PRO MPD diffractometer from Malvern PANalytical (Malvern, UK). SEM was used to assess the morphology, size, and aspect ratio of the fibers obtained under different synthesis conditions and after annealing. This information is crucial for understanding how synthesis parameters influence filler geometry, which directly affects composite performance through percolation and thermal transport mechanisms. Fiber length was quantified using ImageJ software (v1.53) by applying Otsu's automatic thresholding method to SEM images, followed by particle analysis, ensuring that at least 200 individual fibers were measured for each experimental condition. XRD was employed to identify the crystalline phases formed during synthesis and post-annealing treatments. It allows us to confirm the successful formation of the desired AACH precursor and to track its phase transformation into α-Al_2O_3, the thermodynamically stable phase with the highest thermal conductivity among alumina polymorphs.

The thermal conductivity of the composites was evaluated using a thermal conductivity analyzer, and SEM was additionally used to confirm filler distribution and structuring.

3. Results and Discussion

The hydrothermal synthesis of AACH fiber precursor is an interesting route to the elaboration of α-Al_2O_3 fibers that presents high thermal conductivity. The successful synthesis of these fibers with adequate length is crucial to studying the influence of the filler aspect ratio on the properties of polymer-Al_2O_3 composites. To achieve this goal, we will comprehensively examine the impact of various synthesis parameters on the size distribution of the synthesized fibers. Specifically, we will investigate the influence of stirring, reaction time and temperature, and concentration of aluminum nitrate and urea on the hydrothermal synthesis process. Each of these parameters can significantly affect the morphology, size, and quality of the resulting fibers, making it essential to understand their roles in the synthesis process to optimize the production of AACH fibers.

In parallel, we acknowledge the importance of polyethylene glycol (PEG) which plays an important structure-directing role. PEG molecules act as templates by facilitating the transportation of aluminum ions to crystal nuclei and promoting the formation of specific morphologies through surfactant-induced fiber formation (SIFF) mechanisms [25,31–33]. The polymer chains adsorb onto aluminum hydroxide precursor particles through hydrogen bonding and electrostatic interactions, controlling the nucleation and growth processes that ultimately determine the final fiber architecture [31,32,34]. While extensive research has investigated the influence of PEG molecular weight on alumina morphology [25,31,35], very few studies have systematically explored PEG concentration effects. This research gap exists primarily because molecular weight fundamentally determines the polymer's ability to form micelles and control crystal growth kinetics, making it a more critical parameter than concentration for achieving desired morphologies [25,35]. The templating mechanism of PEG operates through the formation of micellar structures that establish controlled microenvironments for aluminum hydroxide precursor nucleation and growth. Our selection of PEG6000 reflects a balanced approach that optimizes both processing characteristics and templating performance for our specific synthesis conditions. The influence of PEG

molecular weight, although recognized as a key parameter, lies beyond the scope of the present study and will be investigated in future work.

In line with the objectives of this study, which focuses on the morphology of the fibers, the yield of Al_2O_3 fibers under different synthesis conditions is not addressed in this study. The primary focus is placed on understanding the influence of synthesis parameters on the main characteristics that most directly govern the fibers' thermal performance in composite applications. A detailed investigation of yield variations will be considered in future work aimed at optimizing process scalability.

In addition to the synthesis process, the annealing procedure will be studied, which is vital for the transformation of fibers into the desired and stable α-phase alumina. This step is necessary to ensure optimal intrinsic properties of the fibers, and thus, the resulting performance of fiber-filled composites in subsequent investigations. We will discuss the annealing conditions and their impact on the phase transformation, crystallinity, and microstructure of the Al_2O_3 fibers.

Table 1 summarizes the different hydrothermal syntheses carried out and details the related parameters considered.

Table 1. Summary of the hydrothermal synthesis parameters. Parameters shown in bold were those specifically varied in each synthesis series.

	Time	Temperature	[$Al(NO_3)_3$]	[urea]	[PEG]	Stirring	Parameter Studied
Synthesis 1	24 h	140 °C	0.6 M	5.5 M	1.5 mM	**OFF**	Solubility Kinetics
Synthesis 2	24 h	140 °C	0.6 M	5.5 M	1.5 mM	**250 rpm**	
Synthesis A	24 h	140 °C	**0.08 M**	5.5 M	1.5 mM	250 rpm	Influence of $Al(NO_3)_3$
Synthesis B	24 h	140 °C	**0.15 M**	5.5 M	1.5 mM	250 rpm	
Synthesis C	24 h	140 °C	**0.3 M**	5.5 M	1.5 mM	250 rpm	
Synthesis D	24 h	140 °C	**0.6 M**	5.5 M	1.5 mM	250 rpm	
Synthesis E	24 h	140 °C	0.3 M	**2.7 M**	1.5 mM	250 rpm	Influence of urea
Synthesis F	24 h	140 °C	0.3 M	**5.5 M**	1.5 mM	250 rpm	
Synthesis G	24 h	140 °C	0.3 M	**11 M**	1.5 mM	250 rpm	
Synthesis H	24 h	140 °C	0.3 M	**22 M**	1.5 mM	250 rpm	
Synthesis I	**3 h**	140 °C	0.3 M	5.5 M	1.5 mM	250 rpm	Influence of reaction time
Synthesis J	**6 h**	140 °C	0.3 M	5.5 M	1.5 mM	250 rpm	
Synthesis K	**12 h**	140 °C	0.3 M	5.5 M	1.5 mM	250 rpm	
Synthesis L	**24 h**	140 °C	0.3 M	5.5 M	1.5 mM	250 rpm	
Synthesis M	**48 h**	140 °C	0.3 M	5.5 M	1.5 mM	250 rpm	
Synthesis N	**72 h**	140 °C	0.3 M	5.5 M	1.5 mM	250 rpm	
Synthesis O	24 h	**120 °C**	0.3 M	5.5 M	1.5 mM	250 rpm	Influence of reaction Temperature
Synthesis P	24 h	**140 °C**	0.3 M	5.5 M	1.5 mM	250 rpm	
Synthesis Q	24 h	**160 °C**	0.3 M	5.5 M	1.5 mM	250 rpm	

3.1. Improving Solubility Kinetics in the Synthesis Process

AACH fibers can be synthesized through a hydrothermal reaction between aluminum nitrate nonahydrate ($Al(NO_3)_3 \cdot 9H_2O$) and urea ($CO(NH_2)_2$) in an aqueous medium. Polyethylene glycol (PEG) is typically added, as it plays the role of a template for the growth of fibers [36]. To investigate the role of solubility kinetics on the chemical reaction leading to the formation of these fibers, two identical synthesis processes were conducted; the

first was in the presence of magnetic stirring during the whole process, and the second in its absence.

Figure 2A,B display SEM micrographs of the obtained fibers from synthesis A and B, respectively, both at a magnification of 1800.

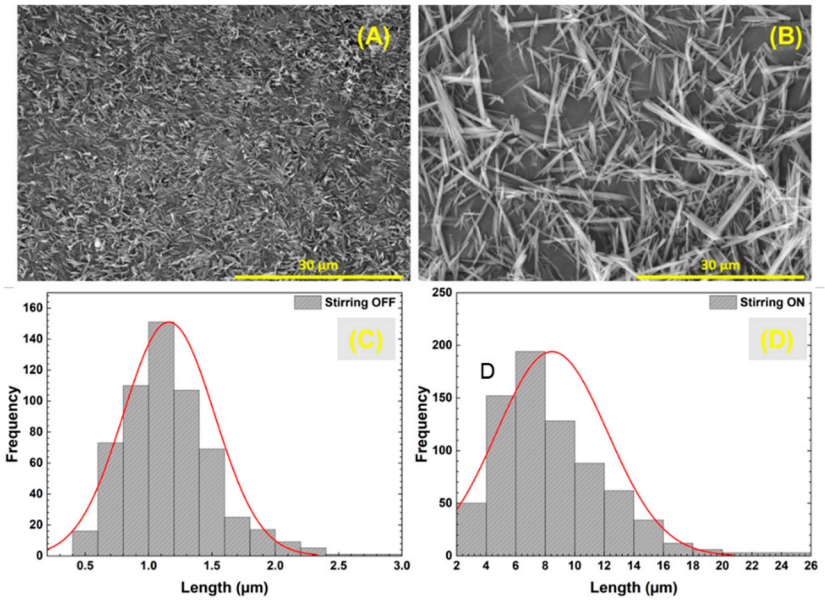

Figure 2. SEM micrograph of the synthesized AACH fibers: (**A**) Without stirring, (**B**) 250 rpm stirring and length distribution calculated for AACH fibers synthesized, (**C**) Without stirring, and (**D**) under 250 rpm stirring.

The findings reveal a marked distinction between synthesis (1) and (2), where the presence of stirring substantially enhances fiber length. This improvement could be attributed to accelerated solubility kinetics of the various reactants in the presence of stirring. Mechanistically, stirring promotes rapid mass transport of reactant species throughout the solution, reducing local concentration gradients and ensuring more uniform supersaturation conditions necessary for controlled nucleation and growth. It prevents the formation of localized regions with depleted reactant concentrations, which would otherwise lead to irregular nucleation patterns and shorter fiber lengths. Additionally, stirring facilitates the removal of reaction byproducts from the crystal–solution interface, maintaining the driving force for continued crystal growth along the preferred crystallographic directions. In the considered application of thermally conductive composites, increased fiber lengths lead to more effective thermally conductive pathways, reduced percolation threshold, diminished thermal resistance interfaces, and ultimately, higher effective thermal conductivities. To quantify the differences between both syntheses, fiber length measurements were carried out using the ImageJ software. The resulting values were used to plot the fiber length distribution (inserts of Figure 2C,D).

The results reveal a narrower length distribution for synthesis A, characterized by a median fiber length of 1.2 µm. In contrast, synthesis 1, employing a 250-rpm stirring, reveals a wider distribution with a considerably higher median length of 8.5 µm, more than 5 times longer than synthesis 2. In view of these results, further investigation into parameter optimization will be conducted using a 250-rpm stirring.

The crystallographic structures were established from XRD analysis performed at room temperature on both synthesis A and B fibers (Figure 3). An identical sharp diffraction peak for both considered syntheses demonstrates the high crystallinity of the fibers. Moreover, this observation suggests that stirring does not alter significantly the outcome from a crystallographic perspective. All peaks can be indexed to the crystalline AACH component,

with a composition of $NH_4[Al(OOH)HCO_3]$, in agreement with the diffraction patterns found in the literature [25,36].

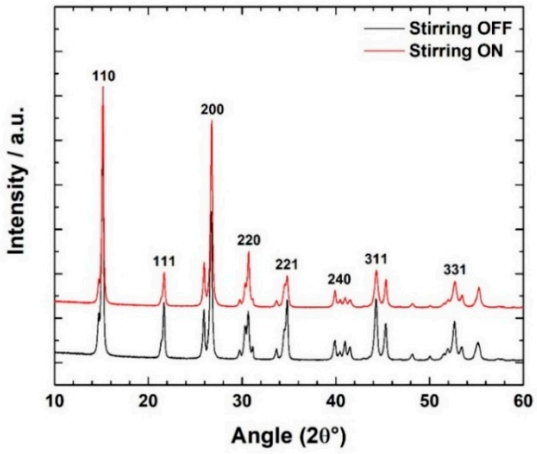

Figure 3. XRD patterns of the synthesized fibers with and without stirring.

3.2. Influence of the Hydrothermal Synthesis Reagents

Aluminum nitrate nonahydrate is one of the most important components in the considered chemical synthesis, as it reacts with NH_3 and CO_2, supplied by urea, to form the AACH fibers in accordance with the following reaction [36]:

$$Al(NO_3)_3 + 4NH_3 + CO_2 + 3H_2O \rightarrow NH_4[Al(OOH)HCO_3] \downarrow + 3NH_4NO_3 \quad (1)$$

Thus, its concentration is a key parameter in the optimization of the chemical synthesis of fibers. To investigate the influence of aluminum nitrate on the length distribution of microfibers, 4 syntheses were conducted with 4 various $Al(NO_3)_3$ concentrations ranging from 0.08 M to 0.6 M. Table 1 summarizes the key parameters of the 4 considered syntheses.

The resulting fibers were characterized through SEM observations. Figure 4A–D show the corresponding SEM micrographs of fibers from the various considered reactions, at a magnification of 2000×. A slight improvement in fiber length is pointed out as the concentration of $Al(NO_3)_3$ increases. To quantify the differences between the resulting fibers, length measurements were conducted using ImageJ. The resulting values were used to plot the length distribution, displayed in Figure 5. It is important to highlight that XRD analysis on the resulting fibers of these syntheses confirmed the crystallographic structure of AACH.

The results reveal a progressive increase in average fiber length with the increasing concentration, yielding median values of 4.7 µm, 6.3 µm, 7.4 µm, and 8.5 µm, respectively. Nevertheless, synthesis C, corresponding to 0.3 M, results in a wider distribution. Consequently, while it contains a greater number of smaller fibers, it also displays the largest fibers measured, reaching lengths up to 20 µm. Bai et al. investigated the influence of aluminum nitrate concentration on the resulting fibers. They observed that an increase in the aluminum salt concentration led to higher fiber width [37]. This effect was related, in their study, to the ion strength of the synthesis system. Quantitatively, Bai et al. reported fiber lengths ranging from 8 to 10 µm with an aluminum concentration of 0.6 M, in good agreement with the value reported in this study. The mechanism proposed by Bai et al. focuses primarily on ionic strength effects, which is consistent with our electrical double-layer compression model.

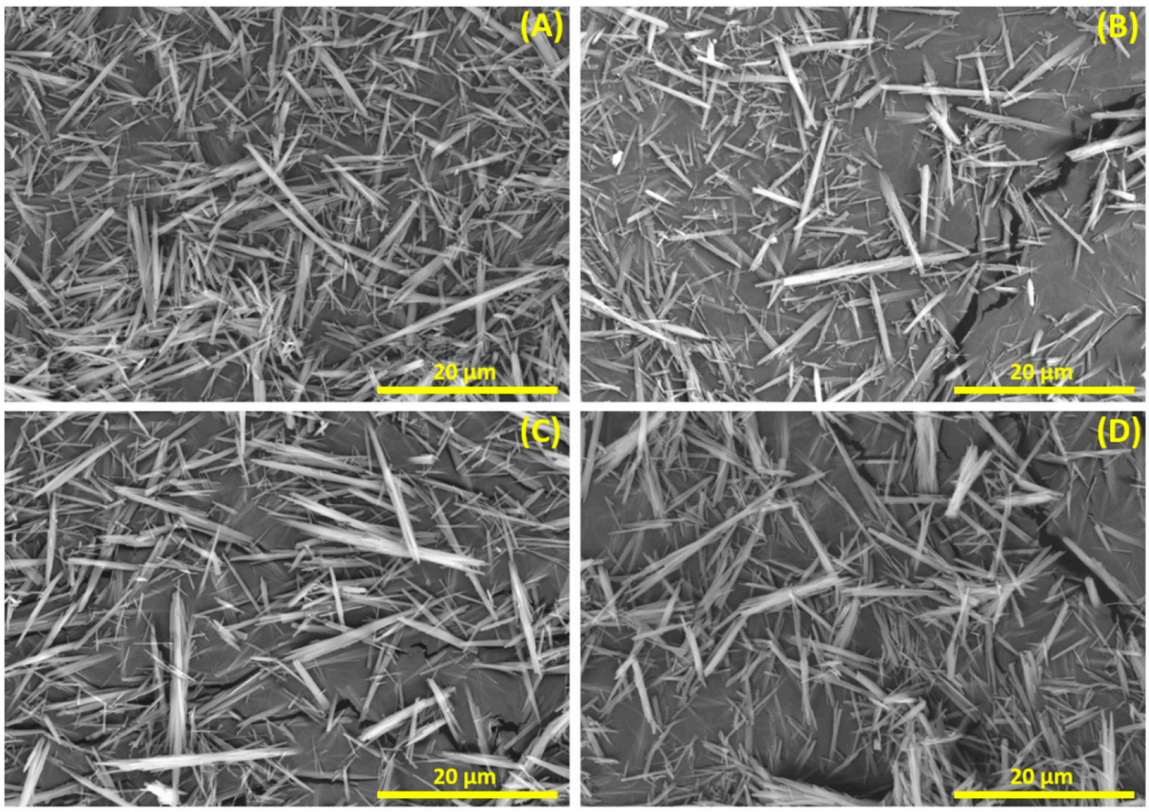

Figure 4. SEM micrographs of AACH fibers resulting from different syntheses with different $Al(NO_3)_3$ concentrations: (**A**) 0.08 M, (**B**) 0.15 M, (**C**) 0.3 M, and (**D**) 0.6 M.

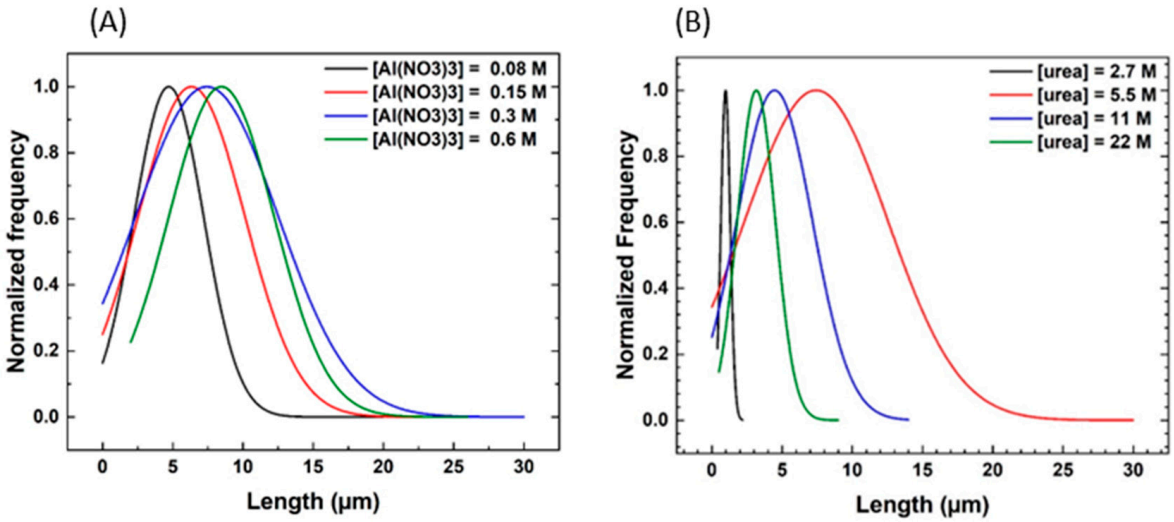

Figure 5. Fiber length distribution as a function of synthesis parameters (**A**) $Al(NO_3)_3$ concentration (**B**) urea concentration.

A higher concentration of aluminum salt results in the presence of more ions, thus increasing the ion strength of the solution. As the reaction between aluminum nitrate and urea starts, primary particles of AACH are initially formed. These primary particles carry charges on their surface that attract oppositely charged ions, creating an electrical double layer. As the aluminum salt concentration increases, the electrical double layer is compressed due to the electrical interaction between opposite charge ions. This compression promotes rapid growth into larger precipitates, thus leading to longer and thicker fibers [37]. The electrical double layer compression follows the Debye–Hückel theory, where increased

ionic strength reduces the thickness of the diffuse layer [38]. This reduction in electrostatic repulsion facilitates the oriented attachment of primary AACH particles along their crystallographic axes, promoting one-dimensional growth into fibrous morphologies [29,39]. Furthermore, the higher aluminum concentration provides increased driving force for nucleation through elevated supersaturation, leading to the formation of more primary nuclei that subsequently undergo oriented attachment and Ostwald ripening processes to form longer, more uniform fibers [40,41]. Another study, reported by Lin et al. [42], investigated extensively the kinetics of the hydrothermal synthesis of AACH microfibers. Their findings revealed an increase in fiber dimensions with the increasing concentration of aluminum nitrate. This observation was attributed to the supersaturation of Al ions, resulting in a stronger driving force of axial growth and the dissolution of radial substances [42].

In addition to aluminum nitrate, urea ($CO(NH_2)_2$) is a major reactant in AACH synthesis, as its dissolution provides the HCO_3^- and NH_4^+ ions necessary for the formation of this component [42]. To investigate the influence of urea concentration, four syntheses were conducted with varying urea concentrations. Table 1 summarizes the key parameters of the syntheses considered.

The resulting fibers were characterized through SEM observations. Figure 6A–D display the corresponding SEM micrographs of fibers from the various investigated reactions, at a magnification of 2000×. The results demonstrate significant differences between various urea concentrations. Figure 6A shows very small and agglomerated fibers due to the minimal presence of urea. As the concentration increases beyond 5.5 M, the resulting fibers exhibit decreasing length, illustrated by Figure 6C,D. The qualitative assessment suggests that the optimal urea concentration is 5.5 M. To quantify these differences, length measurements were carried out to plot the length distribution, represented in Figure 5B. The findings suggest that a low concentration of urea (i.e., 2.7 M) results in extremely small fibers, with a median length of 0.9 µm. Indeed, an insufficient concentration of urea fails to provide enough HCO_3^- and NH_4^+ ions to support the one-dimensional self-assembly growth of AACH fibers [37,42]. This limitation occurs because the kinetics of urea decomposition at hydrothermal temperatures determines the rate of ion release, and insufficient urea concentration results in ion-starved conditions that favor the formation of thermodynamically stable but morphologically unfavorable AlOOH phases rather than the kinetically favored one-dimensional AACH structures [28]. The optimal urea concentration ensures a balance between nucleation and growth rates, where controlled supersaturation promotes oriented attachment mechanisms that drive preferential growth along the crystallographic c-axis of AACH [29,39]. The results also show a narrower distribution and a decrease in the median size as urea concentration surpasses 5.5 M.

Consequently, average values experience a reduction from the optimal 7.4 µm to 4.5 µm and 3.1 µm, respectively. While many studies have reported an optimal urea concentration neighboring 6 M [25,37,42], few studies have investigated concentrations beyond 20 M. As urea is responsible for providing HCO_3^- and NH_4^+ ions, which regulate the nucleation and condensation rates by controlling system pH [25,37], an excessive concentration of urea may result in a disproportionate increase in nucleation rates, lacking sufficient Al ions to complete appropriate growth, ultimately yielding shorter and more numerous fibers.

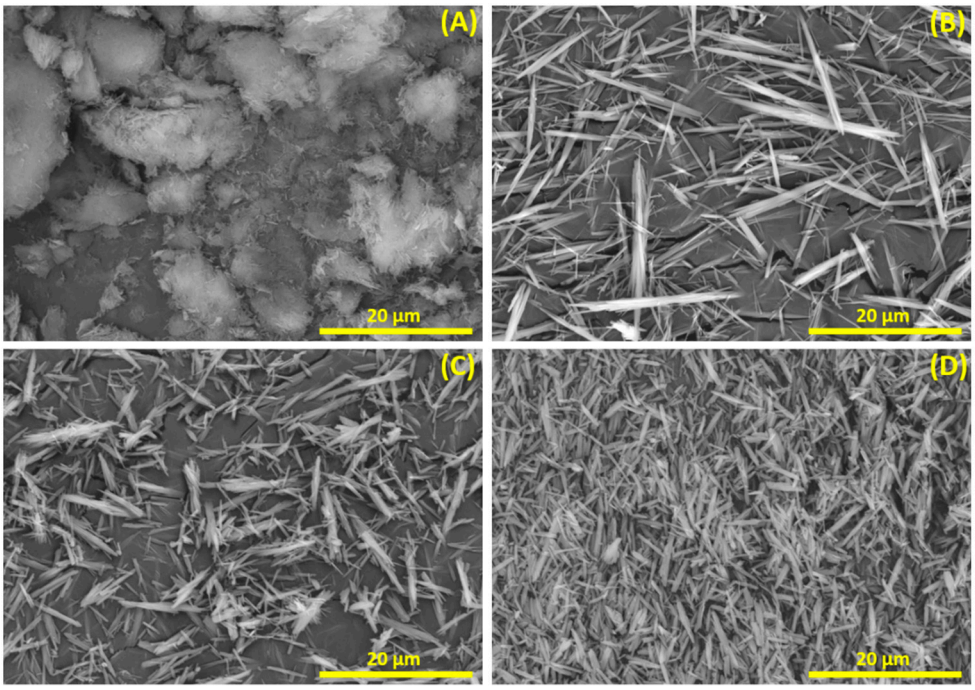

Figure 6. SEM micrographs of AACH fibers resulting from different syntheses with different urea concentrations: (**A**) 2.7 M, (**B**) 5.5 M, (**C**) 11 M, and (**D**) 22 M.

3.3. Time-Temperature Dependence of the Hydrothermal Reaction

The reaction time plays a crucial role in controlling the morphology, size, and quality of the resulting AACH fibers. However, there is a close relationship between time and temperature, as is the case with most chemical reactions. This concept, called "time–temperature equivalence" or "time–temperature superposition", is based on the idea that the effect of varying temperature on the rate of a chemical reaction can be compensated for, to a certain degree, by the time scale of the reaction, and vice versa [43].

Numerous scientific papers have reported successful AACH fiber synthesis at various reaction times, ranging from 7 h to 24 h [28,35,44], while many others have specifically investigated the influence of time on the morphology and size of the resulting fibers [25,42,45]. However, few studies have investigated reaction times longer than 24 h. In the current study, reaction times ranging from 3 h to 72 h will be investigated. Table 1 summarizes the key parameters of the considered reaction syntheses. The resulting fibers were characterized through SEM observations. Figure 7A–F show the corresponding SEM micrographs of AACH fibers from the aforementioned syntheses, at a magnification of 1500×.

The results show that a reaction time of 12 h and below is insufficient to yield adequate fiber growth, whereas a 24 h reaction time and above leads to similar fiber lengths from a qualitative perspective. It is worth mentioning that increasing the reaction temperature would reduce the minimum time required to obtain fully grown AACH fibers, in line with the time–temperature equivalence. In fact, Lin et al. have reported a similar study conducted at 180 °C, wherein a 4 h reaction time was sufficient to obtain microfibers [42]. The difference between Lin et al.'s synthesis conditions (4 h at 180 °C) and ours (24 h at 140 °C) clearly illustrates the time–temperature equivalence principle in AACH synthesis, as further supported by the comparable microfiber lengths obtained: 7 µm for Lin et al. and 8 µm in this study.

To establish their chemical and crystallographic structure, XRD analysis was conducted at room temperature on the resulting samples of the aforementioned syntheses.

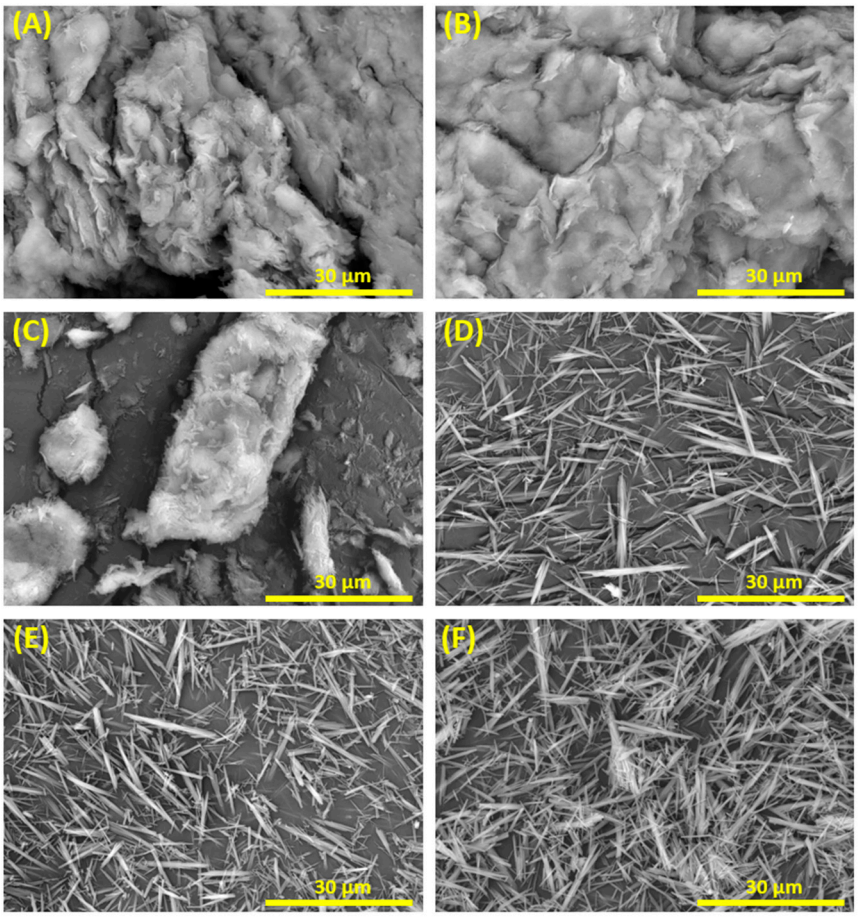

Figure 7. SEM micrographs of AACH fibers resulting from different syntheses with different reaction times: (**A**) 3 h, (**B**) 6 h, (**C**) 12 h, (**D**) 24 h, (**E**) 48 h, (**F**) 72 h.

For more clarity, only the products of syntheses with reaction times of 24 h or less will be presented. Figure 8A displays the diffraction patterns of the samples considered (i.e., 3 h, 6 h, 12 h, and 24 h reaction times). The results outline the emergence of a distinct crystallographic phase for reaction times below 12 h. All diffraction peaks can be indexed to aluminum oxyhydroxide (AlOOH), commonly referred to as boehmite [46]. The XRD pattern for a 12 h reaction time synthesis indicates a minor presence of AACH diffraction peaks, signifying a mixture with boehmite. Reaction times of 24 h or higher result in a pure AACH crystallographic structure. A similar result has been observed in the comprehensive study reported by Lin et al., wherein both AACH and boehmite were identified in reaction times below 2 h at 180 °C [42]. This phenomenon is associated with the AACH growth mechanism during hydrothermal synthesis. In the initial stages of the reaction, AlOOH aggregates are formed due to the low adsorption capacity of HCO_3^- and NH_4^+ ions originating from the hydrolysis of urea. As the reaction progresses, the spherically aggregated particles transform into flakes, which exhibit lower Gibbs free energy, thus enhancing the likelihood of oriented attachment. Smaller AlOOH spheres are preferentially adsorbed along the axis of AACH microfibers [42]. This transformation involves Ostwald ripening, where smaller AlOOH particles dissolve and their constituent ions recrystallize as AACH nuclei in the presence of sufficient HCO_3^- and NH_4^+ concentrations. Consequently, when the reaction time is shortened, the synthesis does not reach the stage where AACH formation occurs, resulting in the presence of AlOOH in the final reaction product. The critical time scale for this phase transformation is determined by the kinetic competition between AlOOH dissolution and AACH nucleation rates, which are governed by temperature, urea decomposition kinetics, and the local supersaturation of aluminum species.

Length measurements were also conducted on the SEM micrographs for reaction times of 24 h and higher, to plot the length distribution of the resulting fibers, represented in Figure 8B. The results reveal that all three reaction times yield an almost similar fiber length distribution, with a median length approximating 7.5 µm. Consequently, this observation suggests that beyond the adequate threshold of 24 h, at the considered temperature of 140 °C, additional reaction time does not appear to considerably improve the outcome of the synthesis.

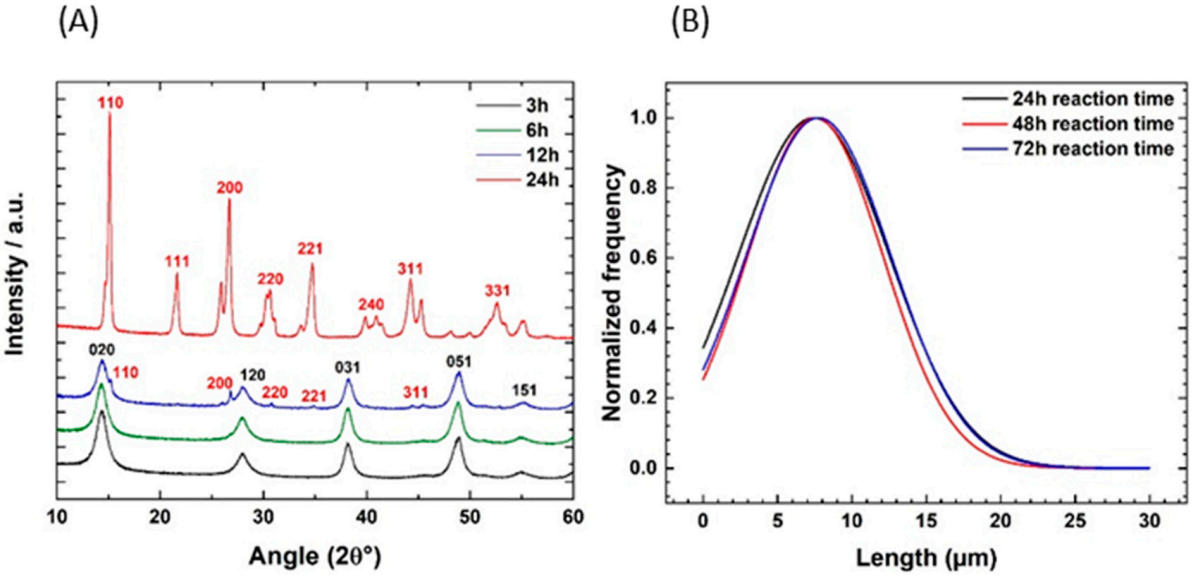

Figure 8. (**A**) XRD pattern of the products of various syntheses with a reaction time ranging from 3 h to 24 h and (**B**) Fiber length distribution resulting from the various syntheses investigating the influence of the reaction time.

Reaction temperature plays a crucial role in the synthesis, as it regulates the kinetics of urea hydrolysis, releasing HCO_3^- and NH_4^+ ions that support the one-dimensional self-assembly growth of AACH. To investigate the influence of temperature on the resulting fibers, three syntheses were carried out with temperatures ranging from 120 °C to 160 °C. The resulting fibers were characterized through SEM observations. Figure 9A–C show the corresponding SEM micrographs of fibers from the various considered reactions, at a magnification of 1500. The results reveal substantial differences in AACH fiber formation as a function of temperature, where 120 °C leads to shorter fibers with a narrower length distribution, while 160 °C results in a wider distribution with a higher presence of smaller fibers. Qualitatively, a 140 °C reaction temperature appears to be the optimal temperature out of the considered range.

Quantitatively, the findings confirm that 140 °C is the optimal temperature, as it results in larger fibers, with a median length of 7.4 µm compared to the average 4.1 µm and 6 µm for 120 °C and 160 °C, respectively. It is essential to note that these results are only applicable to the considered reaction time of 24 h, in accordance with the time–temperature equivalence. Thus, a shorter or longer reaction time may change the optimal temperature value. Indeed, Lin et al. reported an optimal temperature of 180 °C for a reaction time of 8 h [42].

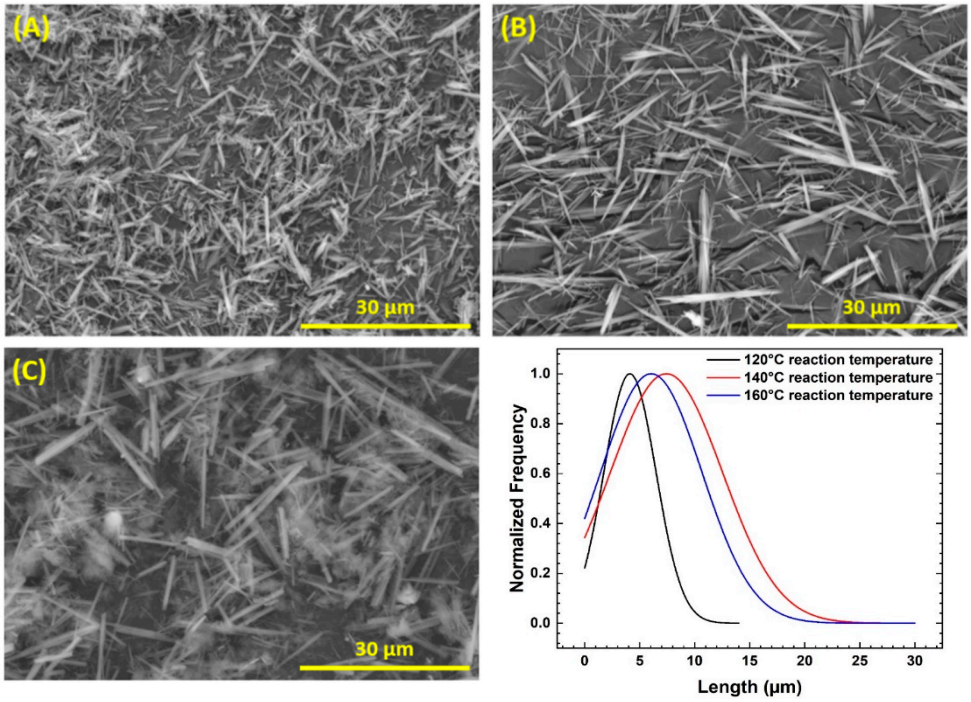

Figure 9. SEM micrographs of AACH fibers resulting from different syntheses with varying reaction temperatures: (**A**) 120 °C, (**B**) 140 °C, and (**C**) 160 °C and Fiber length distribution resulting from AACH syntheses with varying reaction temperature.

At low temperatures, small fibers are observed due to slow urea hydrolysis, providing insufficient HCO_3^- and NH_4^+ ions, whereas sustained and ordered one-dimensional growth occurs in mid-range temperatures [42]. The temperature dependence of fiber growth follows Arrhenius kinetics for both urea decomposition and crystal growth processes. At temperatures below 120 °C, the activation energy barrier for urea hydrolysis limits the rate of ion release, creating ion-starved conditions that favor the formation of short, irregular particles rather than extended fibers. The optimal temperature range (140–160 °C) provides sufficient thermal energy to accelerate urea decomposition while maintaining controlled supersaturation conditions that promote oriented attachment and one-dimensional growth. High temperatures induce chaotic growth as well as decomposition of AACH back into AlOOH (boehmite) [42]. At excessive temperatures (>160 °C), several competing mechanisms occur simultaneously: (1) rapid urea decomposition creates high supersaturation leading to burst nucleation and irregular growth, (2) thermal instability of AACH causes its decomposition back to the more thermodynamically stable AlOOH phase, and (3) enhanced molecular motion disrupts the oriented attachment process necessary for fiber formation. The presence of boehmite in the 160 °C synthesis was confirmed through XRD analysis, presented in Figure 10. This phase transformation demonstrates the narrow kinetic window for AACH fiber formation, where optimal conditions require precise control over temperature, reaction time, and precursor concentrations to maintain the delicate balance between nucleation, growth, and phase stability. Similar findings have been reported by Lin et al. in their parametric study, where they observed the presence of boehmite at 220 °C for a reaction time of 8 h, which further confirms the time–temperature equivalence [42]. Li et al. also reported the presence of boehmite at 150 °C for a 24 h synthesis time [47].

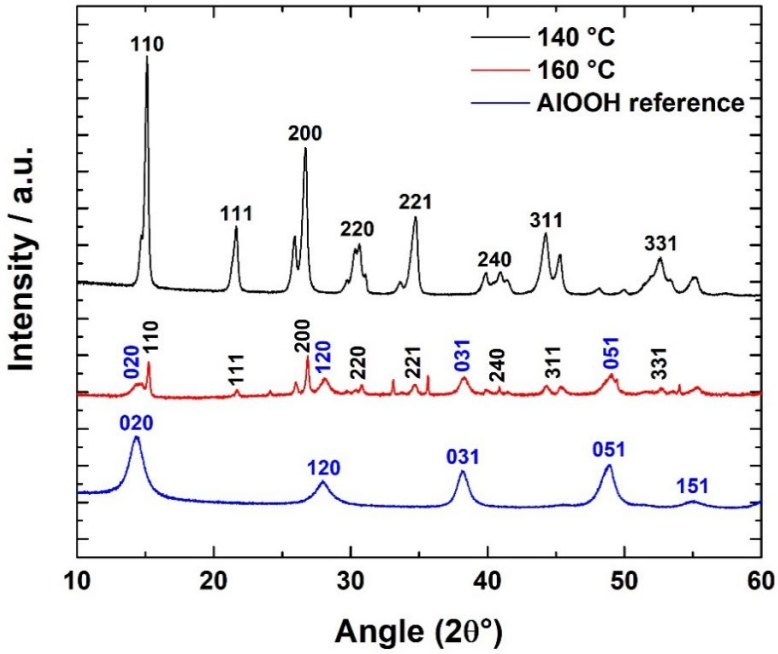

Figure 10. XRD pattern of the product of 140 °C and 160 °C AACH synthesis with an AlOOH reference.

3.4. From AACH to α-Al_2O_3 Fibers

Alumina (Al_2O_3) can be obtained from the thermal decomposition of AACH at high temperatures, by releasing H_2O, NH_3, and CO_2, according to the following reactions [48,49]:

$$NH_4[Al(OOH)HCO_3] \rightarrow AlOOH + CO_2 + NH_3 + H_2O \quad (2)$$

$$2AlOOH \rightarrow Al_2O_3 + H_2O \quad (3)$$

The resulting alumina phase is dependent on the annealing temperature. The fibers derived from the previously described synthesis were subjected to an initial annealing process at 900 °C for 4 h at a heating rate of 3 °C/min. Figure 11 shows the XRD analysis of the consequent structure following the annealing procedure.

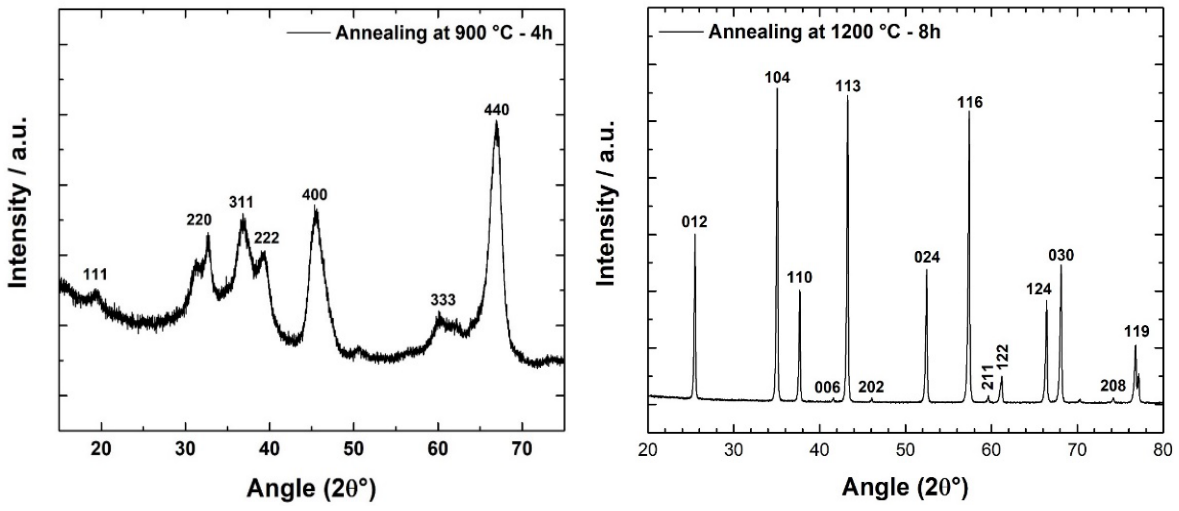

Figure 11. (**Left**) XRD pattern of γ -Al_2O_3 (annealed AACH at 900 °C for 4 h) and (**Right**) α-Al_2O_3 annealed at 1200 °C for 8 h.

XRD patterns of annealed fibers highlight the presence of a crystallographic phase, different from that of AACH. All diffraction peaks can be indexed to γ-Al_2O_3 [50], confirming a successful conversion of AACH into Al_2O_3 through the annealing process. However, the current γ-phase is undesired from a thermal conductivity standpoint, as it is not as crystalline and well-performing as other alumina phases, namely, the thermodynamically stable α-Al_2O_3 [51]. To obtain a higher-performing crystallographic phase of alumina, the resulting γ-Al_2O_3 was subjected to a second annealing process at 1200 °C for 8 h with a heating rate of 3 °C/min. XRD analysis of the consequent structure (Figure 11) reveals a highly crystalline structure. All diffraction peaks can be indexed to α-Al_2O_3 [52], also referred to as "corundum". Numerous studies have undertaken similar calcination and annealing processes of AACH and have reported identical crystallographic structures [53–57].

To establish the impact of the annealing process on their size and shape, the obtained α-Al_2O_3 fibers were characterized through microscopic observations and fiber size distribution analysis. SEM micrograph (Figure 12) of the α-Al_2O_3 fibers at a magnification of 1500. The SEM picture highlights the presence of fibers with adequate length and aspect ratio. Their size distribution appears to be more homogeneous, which represents an improvement. These findings indicate that the annealing process that yields α-Al_2O_3 does not significantly alter the shape of the fibers.

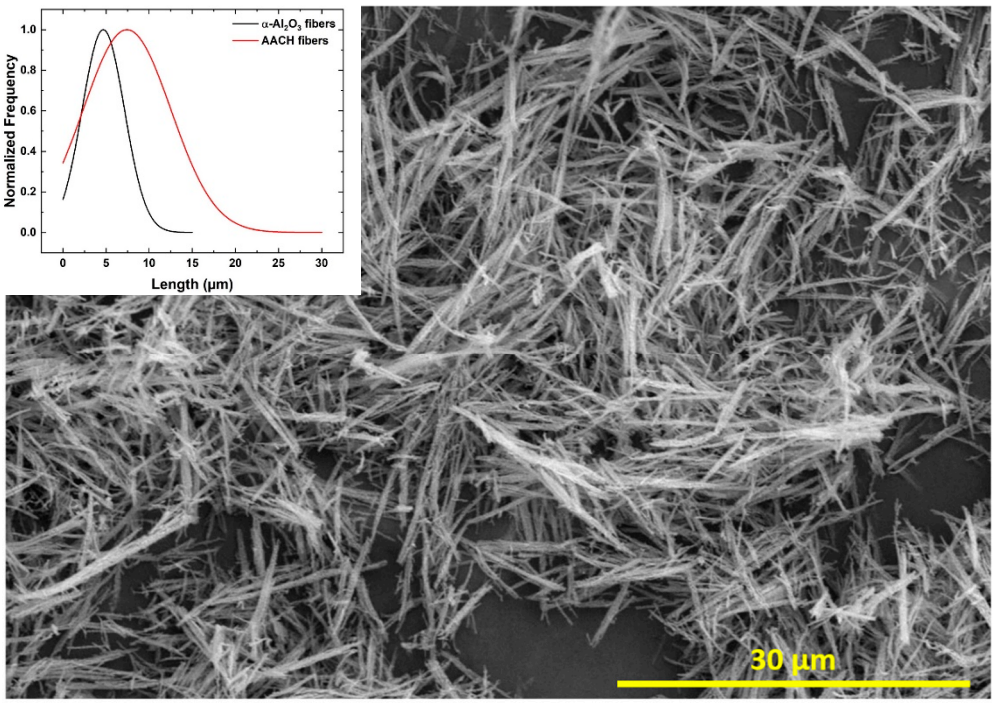

Figure 12. SEM picture of α-Al_2O_3 fibers resulting from the annealing process and (insert) Length distribution of both AACH and α-Al_2O_3 fibers.

The annealing process yields highly crystalline α-Al_2O_3 fibers, as confirmed by XRD analysis, and results in densification and reduced porosity as observed by SEM. These microstructural changes are essential for optimizing the thermal conductivity of fiber-filled composites, as the α-phase provides superior intrinsic thermal properties and the reduced porosity minimizes thermal barriers.

Size distribution study (Figure 12-insert) shows a narrower distribution of fiber length for α-Al_2O_3 fibers compared to their AACH predecessors. It also highlights a decrease in fiber length, with a median value of 4.7 μm compared to the initial 7.4 μm, a 36% decrease due to the annealing process and the changes in the crystallographic structure. The observed reduction in size is not atypical after a structural change from AACH to

γ-Al_2O_3 or α-Al_2O_3 and has been reported in the literature [25,37]. The resulting α-Al_2O_3 will allow an insightful investigation of the influence of the aspect ratio on the properties of polymer-Al_2O_3 composites, both in their structured and unstructured configurations.

3.5. Development of Hybrid PDMS-Based Composites from α-Al_2O_3 Fibers

The significance of studying the effect of filler aspect ratio lies in its potential to pave the way for new possibilities of optimizing composite properties, such as filler shape hybridization. By understanding how fillers' aspect ratio impacts a composite's performance, it becomes possible to tailor the material's properties to specific applications and operating conditions. This subchapter aims to investigate the impact of filler aspect ratio on the properties of PDMS-Al_2O_3 composites by comparing the use of Al_2O_3 fibers and Al_2O_3 spherical particles.

Two composite types will be considered: PDMS-Al_2O_3 fiber composites, which incorporate the Al_2O_3 fibers, and PDMS-Al_2O_3 particle composites, which use Al_2O_3 spherical particles with a 2 µm diameter. The investigation will include a study of dielectrophoretic structuring to highlight the effect of the structure on both filler types and the resulting composite properties. Given the limited scale of production of the Al_2O_3 fibers, a low volume fraction ϕ = 5% of fibers inside the sPDMS matrix has been considered. Composite elaboration and structuring optimization will be carried out according to the optimal conditions previously described in [6] (i.e., 4 kV/mm amplitude and 1 Hz frequency).

In order to establish successful fiber structuring under the considered electric field, SEM observations were conducted on cured films made from volume fraction ϕ = 5% of fiber-filled PDMS-Al_2O_3 composites, both structured and unstructured. Figure 13A,B show the SEM images of both composites, respectively. The results reveal significant structural differences between the structured and unstructured composites.

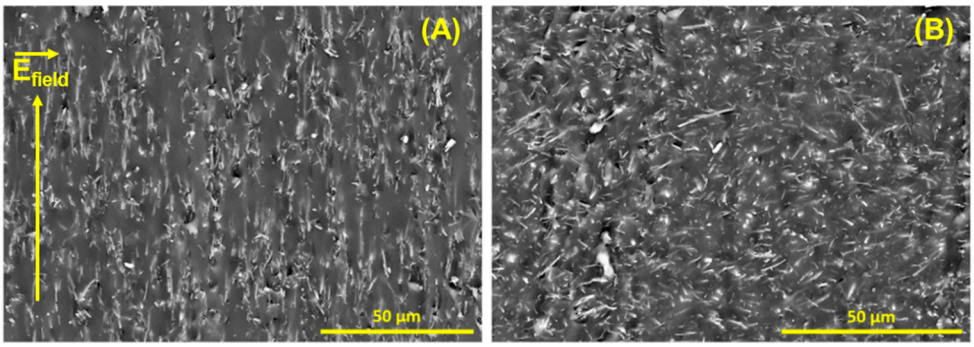

Figure 13. SEM micrographs of fiber-filled PDMS-Al_2O_3 composites with a volume fraction ϕ = 5% of fiber-filled PDMS-Al_2O_3 composites: (**A**) Structured, (**B**) Unstructured.

The structured composite displays Al_2O_3 fibers oriented and aligned along the z-direction (i.e., the electric field's direction). Because of their shape, the orientation of spherical particles is irrelevant; only their alignment influences the composite properties. In contrast, in the case of fibers, both alignment (i.e., the formation of continuous pathways) and orientation play a role in the resulting composite performance. This constitutes an additional advantage of coupling both dielectrophoretic structuring and enhanced filler aspect ratio. The orientation angle of particles related to the electric field direction was calculated from ImageJ software and plotted in Figure 14. Composites with random structure (unstructured) present a dominant transversal fiber orientation (i.e., perpendicular to $\vec{g}$) This may be related to the effect of gravity, where, under the gravitational force, the fibers adopt their vertical position of stability. Composites fabricated by dielectrophoretic

alignment of the fibers display a highly anisotropic microstructure, with the fiber orientation strongly concentrated along the direction of the applied electric field.

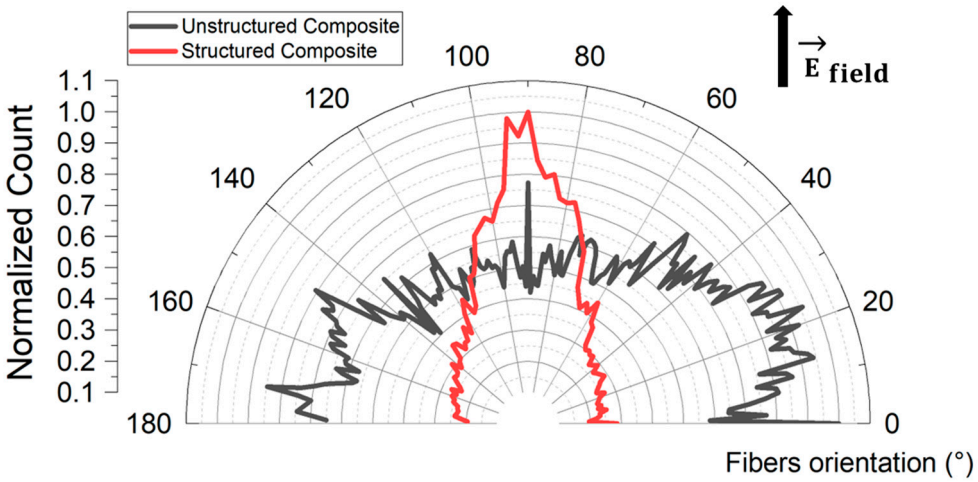

Figure 14. Polar plot of orientation angle of fibers with reference direction perpendicular to electric field direction. The data were extracted from SEM images for unstructured and structured composites and analyzed using ImageJ software.

The Herman's orientation factor is a widely used parameter to quantify the degree of particle alignment within polymer matrices [58]. It is determined from the angle formed between each fiber and the electric field applied during the dielectrophoretic orientation process. In this study, Herman's factor was evaluated according to Equation (4), based on SEM image analysis using ImageJ (Figure 14). The electric field direction (shown in Figure 13A), which corresponds to the thickness of the composite film, was also taken as the reference axis for the calculation of the Herman's factor in the non-oriented sample.

$$f = \frac{3 < cos^2(\theta) > -1}{2} \quad (4)$$

where θ denotes the angle between the longitudinal axis of a fiber and the reference axis (electric field direction). The analysis of this parameter provides a quantitative measure of the orientation state induced by dielectrophoresis. The mean fiber orientation angle decreased from $\theta = 72^\circ \pm 23^\circ$ in the non-oriented structure to $\theta = 0.7^\circ \pm 16^\circ$ in the oriented structure. Unstructured composite exhibits a Herman's factor of $f = -0.36$, indicative of a low degree of alignment, with fibers predominantly oriented perpendicular to the film thickness while structured composites' Herman's factor is $f = 0.97$, corresponding to an almost perfectly aligned structure along the electric field direction.

To assess the influence of filler aspect ratio on the thermal properties of PDMS-Al_2O_3 composites, thermal conductivity measurements were conducted at room temperature on particle-filled and fiber-filled composites with volume fraction $\phi = 5\%$, both structured and unstructured. Figure 15 displays the thermal conductivity of the considered composites. The experimental procedure was fully detailed by Zahhaf et al. [9].

The results indicate an increase in thermal conductivity in fiber-filled composites compared to their particle-filled counterparts, regardless of the considered structure. In fact, the unstructured fiber-filled composite exhibits a 32% increase over its particle-filled counterpart, while in the structured configuration, this increase is as high as 95%. The results also highlight the expected increase in thermal conductivity for structured composites over their unstructured equivalents, regardless of the filler type.

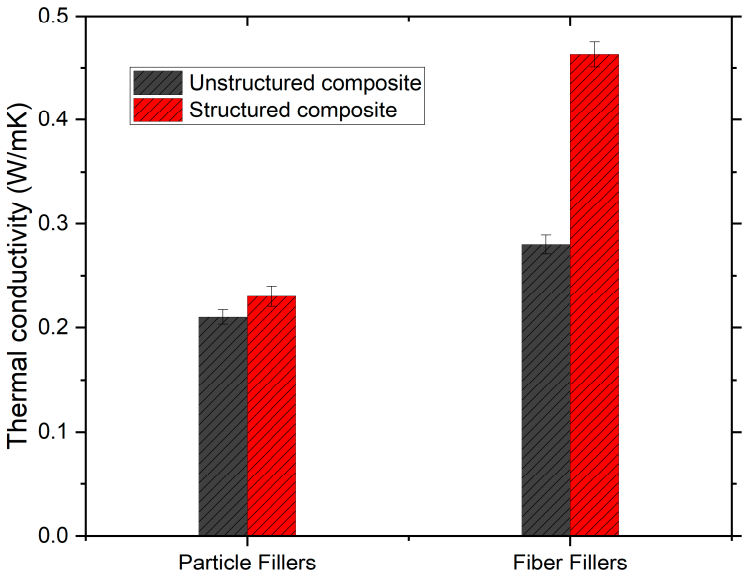

Figure 15. Thermal conductivity of structured and unstructured PDMS-Al_2O_3 composites with a volume fraction ϕ = 5% as a function of their filler's aspect ratio.

The reason behind the enhanced thermal behavior of fiber-filled composites lies in the fillers' high-aspect ratio that influences various important factors in the composite's heat transfer capabilities. Indeed, a high filler aspect ratio results in a lower percolation threshold, leading to a significant increase in thermal conductivity at low filler content [59], particularly in the case of structured composites. Furthermore, the thermal resistance within the composite (i.e., polymer interfaces) decreases as the aspect ratio increases, leading to enhanced thermal performance [60].

4. Conclusions

This study demonstrates a systematic approach for the synthesis of α-Al_2O_3 fibers via hydrothermal processing of ammonium aluminum carbonate hydroxide (AACH) precursors, with a focus on controlling fiber morphology through key process parameters such as reactant concentration, reaction temperature and time, and stirring. The optimized synthesis yielded high-aspect ratio alumina fibers with a refined length distribution, showing a 36% reduction in median length after calcination, resulting in α-Al_2O_3 fibers with a median length of 4.7 µm. These results open perspectives for further optimization, in particular through a systematic investigation of PEG concentration, which may play a role in tailoring the synthesis of alumina fibers. These fibers were successfully integrated into PDMS-based composites, structured through dielectrophoresis and evaluated for thermal conductivity. The results showed that the isotropic fiber-filled composite exhibits a 32% increase over its particle-filled counterpart, while in the structured anisotropic configuration, this increase is as high as 95%.

The experimental results clearly demonstrate the critical role of filler morphology and alignment on thermal conductivity. Fiber-filled composites outperformed particle-filled systems, and dielectrophoretic alignment of the fibers resulted in a significant enhancement of thermal conductivity (i.e., 60% increase) over unstructured counterparts (i.e., 9% increase). This underscores the importance of aspect ratio in optimizing heat transport in polymer-based composites.

Importantly, this work introduces an interesting route to produce ceramic fibers and validates their efficacy in thermally conductive yet electrically insulating composites. These findings provide a framework for the design of next-generation hybrid composites,

where filler geometry and spatial organization can be tailored to meet demanding thermal management requirements in electronic, energy, and advanced packaging applications.

Author Contributions: Conceptualization, O.Z., G.D., F.G. and J.-F.C.; Methodology, O.Z., G.D. and J.-F.C.; Validation, P.-J.C. and J.-F.C.; Formal analysis, O.Z.; Investigation, O.Z., G.D., G.R., M.-Q.L. and J.-F.C.; Resources, F.G.; Writing—original draft, O.Z. and J.-F.C.; Writing—review and editing, G.R., M.-Q.L., P.-J.C. and J.-F.C.; Supervision, F.G., P.-J.C. and J.-F.C.; Funding acquisition, F.G., P.-J.C. and J.-F.C. All authors have read and agreed to the published version of the manuscript.

Funding: This study was funded by the ANRT under grant number CIFRE n°2019/1046 and supported by the Carnot Institute Ingénierie@Lyon.

Institutional Review Board Statement: Not applicable.

Informed Consent Statement: Not applicable.

Data Availability Statement: The original contributions presented in this study are included in the article. Further inquiries can be directed at the corresponding author.

Conflicts of Interest: Author François Grasland was employed by the company GETELEC. The remaining authors declare that the research was conducted in the absence of any commercial or financial relationships that could be construed as a potential conflict of interest.

References

1. Wang, Z.; Wu, Z.; Weng, L.; Ge, S.; Jiang, D.; Huang, M.; Mulvihill, D.M.; Chen, Q.; Guo, Z.; Jazzar, A.; et al. A Roadmap Review of Thermally Conductive Polymer Composites: Critical Factors, Progress, and Prospects. *Adv. Funct. Mater.* **2023**, *33*, 2301549. [CrossRef]
2. Fan, P.; Sun, Z.; Wang, Y.; Chang, H.; Zhang, P.; Yao, S.; Lu, C.; Rao, W.; Liu, J. Nano liquid metal for the preparation of a thermally conductive and electrically insulating material with high stability. *RSC Adv.* **2018**, *8*, 16232–16242. [CrossRef] [PubMed]
3. Gao, Z.; Zhao, Q.; Li, C.; Wang, S.; Dong, L.; Hu, G.-H.; Yang, Q.; Xiong, C. A novel fluid-filler/polymer composite as high-temperature thermally conductive and electrically insulating material. *Compos. Sci. Technol.* **2017**, *150*, 128–134. [CrossRef]
4. Schelling, P.K.; Shi, L.; Goodson, K.E. Managing heat for electronics. *Mater. Today* **2005**, *8*, 30–35. [CrossRef]
5. Ye, M.; Jiang, J.; Zhao, L.; Zhu, H.; Wang, J.; Sun, Z.; Zhang, D.; Li, M.; Zhang, Y. Preparation of Phenolic Epoxy-Based Electronic Packaging Materials with High Thermal Conductivity by Creating an Interfacial Heat Conduction Network. *Polymers* **2025**, *17*, 1507. [CrossRef]
6. Rivière, L.; Caussé, N.; Lonjon, A.; Dantras, É.; Lacabanne, C. Specific heat capacity and thermal conductivity of PEEK/Ag nanoparticles composites determined by Modulated-Temperature Differential Scanning Calorimetry. *Polym. Degrad. Stab.* **2016**, *127*, 98–104. [CrossRef]
7. Coulson, M.; Dantras, E.; Olivier, P.; Gleizes, N.; Lacabanne, C. Thermal conductivity and diffusivity of carbon-reinforced polyetherketoneketone composites. *J. Appl. Polym. Sci.* **2019**, *136*, 47975. [CrossRef]
8. Pornea, A.G.; Dinh, D.K.; Hanif, Z.; Yanar, N.; Choi, K.-I.; Kwak, M.S.; Kim, J. Preparations and Thermal Properties of PDMS-AlN-Al_2O_3 Composites through the Incorporation of Poly(Catechol-Amine)-Modified Boron Nitride Nanotubes. *Nanomaterials* **2024**, *14*, 847. [CrossRef] [PubMed]
9. Zahhaf, O.; D'Ambrogio, G.; Le, M.-Q.; Coativy, G.; Grasland, F.; Cottinet, P.-J.; Capsal, J.-F. Dielectrophoretic alignment of Al_2O_3/PDMS composites: Enhancement of thermal and dielectric properties through structural sedimentation analysis. *Mater. Des.* **2021**, *211*, 110134. [CrossRef]
10. Sun, Y.; Yin, Y.; Mayers, B.T.; Herricks, T.; Xia, Y. Uniform Silver Nanowires Synthesis by Reducing $AgNO_3$ with Ethylene Glycol in the Presence of Seeds and Poly(Vinyl Pyrrolidone). *Chem. Mater.* **2002**, *14*, 4736–4745. [CrossRef]
11. Liu, P.; Gao, S.; Wang, Y.; Zhou, F.; Huang, Y.; Luo, J. Metal-organic polymer coordination materials derived Co/N-doped porous carbon composites for frequency-selective microwave absorption. *Compos. Part B Eng.* **2020**, *202*, 108406. [CrossRef]
12. Liu, P.; Gao, S.; Liu, X.; Huang, Y.; He, W.; Li, Y. Rational construction of hierarchical hollow CuS@CoS_2 nanoboxes with heterogeneous interfaces for high-efficiency microwave absorption materials. *Compos. Part B Eng.* **2020**, *192*, 107992. [CrossRef]
13. Nan, C.-W. Physics of inhomogeneous inorganic materials. *Prog. Mater. Sci.* **1993**, *37*, 1–116. [CrossRef]
14. Newnham, R.E.; Skinner, D.P.; Cross, L.E. Connectivity and piezoelectric-pyroelectric composites. *Mater. Res. Bull.* **1978**, *13*, 525–536. [CrossRef]
15. Wang, J.; Hu, L.; Li, W.; Ouyang, Y.; Bai, L. Development and Perspectives of Thermal Conductive Polymer Composites. *Nanomaterials* **2022**, *12*, 3574. [CrossRef]

16. Lonjon, A.; Caffrey, I.; Carponcin, D.; Dantras, E.; Lacabanne, C. High electrically conductive composites of Polyamide 11 filled with silver nanowires: Nanocomposites processing, mechanical and electrical analysis. *J. Non-Cryst. Solids* **2013**, *376*, 199–204. [CrossRef]
17. Bedel, V.; Lonjon, A.; Dantras, É.; Bouquet, M.; Lacabanne, C. Dynamic electrical and mechanical properties of epoxy/silver nanowires composites. *J. Appl. Polym. Sci.* **2022**, *139*, 51710. [CrossRef]
18. Tan, J.; Zhang, Y. Thermal Conductive Polymer Composites: Recent Progress and Applications. *Molecules* **2024**, *29*, 3572. [CrossRef]
19. Yuan, H.; Wang, Y.; Li, T.; Ma, P.; Zhang, S.; Du, M.; Chen, M.; Dong, W.; Ming, W. Highly thermal conductive and electrically insulating polymer composites based on polydopamine-coated copper nanowire. *Compos. Sci. Technol.* **2018**, *164*, 153–159. [CrossRef]
20. David, C.; Capsal, J.-F.; Laffont, L.; Dantras, E.; Lacabanne, C. Piezoelectric properties of polyamide 11/$NaNbO_3$ nanowire composites. *J. Phys. Appl. Phys.* **2012**, *45*, 415305. [CrossRef]
21. van den Ende, D.A.; Bory, B.F.; Groen, W.A.; van der Zwaag, S. Improving the d33 and g33 properties of 0-3 piezoelectric composites by dielectrophoresis. *J. Appl. Phys.* **2010**, *107*, 024107. [CrossRef]
22. D'Ambrogio, G.; Zahhaf, O.; Le, M.-Q.; Bordet, M.; Lermusiaux, P.; Della Schiava, N.; Liang, R.; Cottinet, P.-J.; Capsal, J.-F. Piezoelectric biosensor for smart cardiovascular grafts based on $NaNbO_3$ fibers/PDMS structured composite. *Mater. Des.* **2022**, *223*, 111195. [CrossRef]
23. Živcová, Z.; Gregorová, E.; Pabst, W.; Smith, D.S.; Michot, A.; Poulier, C. Thermal conductivity of porous alumina ceramics prepared using starch as a pore-forming agent. *J. Eur. Ceram. Soc.* **2009**, *29*, 347–353. [CrossRef]
24. Bharthasaradhi, R.; Nehru, L.C. Structural and phase transition of α-Al_2O_3 powders obtained by co-precipitation method. *Phase Transit.* **2016**, *89*, 77–83. [CrossRef]
25. Zhu, Z.; Liu, H.; Sun, H.; Yang, D. PEG-directed hydrothermal synthesis of multilayered alumina microfibers with mesoporous structures. *Microporous Mesoporous Mater.* **2009**, *123*, 39–44. [CrossRef]
26. Wu, C.; Zhan, L.; Liu, H.; Wang, J.; Liu, W.; Yao, S.; Ma, Y. The oriented growth behavior of α-Al_2O_3 grains in alumina-mullite biphasic fibers. *J. Eur. Ceram. Soc.* **2024**, *44*, 319–327. [CrossRef]
27. Gai, K.; Wang, Q.; Li, J.; Lu, B.; Liang, L.; Tai, J.; Cheng, Y.; Guan, B.; Zhao, T. Studies on the Crystallization Behavior of Al_2O_3-HfO_2 Ceramic Fibers Prepared by Melt-spinning of Polymer Precursors. *J. Eur. Ceram. Soc.* **2023**, *43*, 5587–5595. [CrossRef]
28. Wang, F.; Zhu, J.; Liu, H. Urea controlled hydrothermal synthesis of ammonium aluminum carbonate hydroxide rods. *AIP Adv.* **2018**, *8*, 035103. [CrossRef]
29. Salzmann, B.B.V.; Van Der Sluijs, M.M.; Soligno, G.; Vanmaekelbergh, D. Oriented Attachment: From Natural Crystal Growth to a Materials Engineering Tool. *Acc. Chem. Res.* **2021**, *54*, 787–797. [CrossRef] [PubMed]
30. Zhu, Z.; Sun, H.; Liu, H.; Yang, D. PEG-directed hydrothermal synthesis of alumina nanorods with mesoporous structure via AACH nanorod precursors. *J. Mater. Sci.* **2010**, *45*, 46–50. [CrossRef]
31. Muhammad, A. An Overview of Mesoporous Alumina Synthesis with Controlled Particle Size Distribution and Improved Textural Morphology. *Iran. J. Chem. Chem. Eng.* **2024**, *43*, 522–543. [CrossRef]
32. Sun, Z.-X.; Zheng, T.-T.; Bo, Q.-B.; Du, M.; Forsling, W. Effects of calcination temperature on the pore size and wall crystalline structure of mesoporous alumina. *J. Colloid Interface Sci.* **2008**, *319*, 247–251. [CrossRef] [PubMed]
33. Zhu, H.Y.; Riches, J.D.; Barry, J.C. γ-Alumina Nanofibers Prepared from Aluminum Hydrate with Poly(ethylene oxide) Surfactant. *Chem. Mater.* **2002**, *14*, 2086–2093. [CrossRef]
34. Kim, D.; Jung, J.H.; Ihm, J. Theoretical Study of Aluminum Hydroxide as a Hydrogen-Bonded Layered Material. *Nanomaterials* **2018**, *8*, 375. [CrossRef] [PubMed]
35. Zhu, Z.; Liu, H.; Sun, H.; Yang, D. Surfactant assisted hydrothermal and thermal decomposition synthesis of alumina microfibers with mesoporous structure. *Chem. Eng. J.* **2009**, *155*, 925–930. [CrossRef]
36. Shi, X.; Yang, C.; Zhang, L.; Lu, Z.; Zhu, Y.; Tang, D.; Cui, C.; Zeng, H. Mesoporous alumina microfibers in situ transformation from AACH fibers and the adsorption performance. *J. Nanomater.* **2014**, *2014*, 381235. [CrossRef]
37. Bai, P.; Su, F.; Wu, P.; Wang, L.; Lee, F.Y.; Lv, L.; Yan, Z.F.; Zhao, X.S. Copolymer-controlled homogeneous precipitation for the synthesis of porous microfibers of alumina. *Langmuir* **2007**, *23*, 4599–4605. [CrossRef]
38. Schott, C.M.; Schneider, P.M.; Song, K.-T.; Yu, H.; Götz, R.; Haimerl, F.; Gubanova, E.; Zhou, J.; Schmidt, T.O.; Zhang, Q.; et al. How to Assess and Predict Electrical Double Layer Properties. Implications for Electrocatalysis. *Chem. Rev.* **2024**, *124*, 12391–12462. [CrossRef]
39. Xue, X.; Penn, R.L.; Leite, E.R.; Huang, F.; Lin, Z. Crystal growth by oriented attachment: Kinetic models and control factors. *CrystEngComm* **2014**, *16*, 1419. [CrossRef]
40. Van Westen, T.; Groot, R.D. Effect of Temperature Cycling on Ostwald Ripening. *Cryst. Growth Des.* **2018**, *18*, 4952–4962. [CrossRef]

41. Ouyang, R.; Liu, J.-X.; Li, W.-X. Atomistic Theory of Ostwald Ripening and Disintegration of Supported Metal Particles under Reaction Conditions. *J. Am. Chem. Soc.* **2013**, *135*, 1760–1771. [CrossRef] [PubMed]
42. Lin, J.; Yang, Z.; Zhao, X.; Ji, H.; Peng, C.; Sui, B.; Chen, W.; Zhang, J.; Qian, G.; Zhou, X.; et al. Kinetics and mechanistic insights into the hydrothermal synthesis of alumina microrods. *Chem. Eng. Sci.* **2021**, *244*, 116817. [CrossRef]
43. Atkins, P.; de Paula, J. *Physical Chemistry for the Life Sciences*; Oxford University Press: Oxford, UK, 2006.
44. Liu, H.; Sun, H.; Li, J.; He, X.; Zhu, Z. PH-dependent formation of AACH fibers with tunable diameters and their in situ transformation to alumina nanocrystals with mesoporous structure. *Adv. Powder Technol.* **2012**, *23*, 164–169. [CrossRef]
45. Mirzajany, R.; Alizadeh, M.; Rahimipour, M.R.; Saremi, M. Seed-assisted hydrothermally synthesized AACH as the alumina precursors. *Mater. Chem. Phys.* **2019**, *221*, 188–196. [CrossRef]
46. Hou, H.; Xie, Y.; Yang, Q.; Guo, Q.; Tan, C. Preparation and characterization of γ-AlOOH nanotubes and nanorods. *Nanotechnology* **2005**, *16*, 741–745. [CrossRef]
47. Li, G.; Liu, Y.; Guan, L.; Hu, X.; Liu, C. Meso/macroporous γ-Al_2O_3 fabricated by thermal decomposition of nanorods ammonium aluminium carbonate hydroxide. *Mater. Res. Bull.* **2012**, *47*, 1073–1079. [CrossRef]
48. Parida, K.M.; Pradhan, A.C.; Das, J.; Sahu, N. Synthesis and characterization of nano-sized porous gamma-alumina by control precipitation method. *Mater. Chem. Phys.* **2009**, *113*, 244–248. [CrossRef]
49. Liu, X.; Li, X.; Yan, Z. Facile route to prepare bimodal mesoporous γ-Al_2O_3 as support for highly active CoMo-based hydrodesulfurization catalyst. *Appl. Catal. B Environ.* **2012**, *121–122*, 50–56. [CrossRef]
50. Prins, R. On the structure of γ-Al_2O_3. *J. Catal.* **2020**, *392*, 336–346. [CrossRef]
51. Cheng, J.P.; Liu, T.; Zhang, J.; Wang, B.B.; Ying, J.; Liu, F.; Zhang, X.B. Influence of phase and morphology on thermal conductivity of alumina particle/silicone rubber composites. *Appl. Phys. Mater. Sci. Process.* **2014**, *117*, 1985–1992. [CrossRef]
52. Sadabadi, H.; Aftabtalab, A.; Zafarian, S.; Shaker, S.; Ahmadipour, M.; Venkateswara, K. High purity Alpha Alumina nanoparticle: Synthesis and characterization. *Int. J. Sci. Eng. Res.* **2013**, *4*, 1593–1595.
53. Morinaga, K.; Torikai, T.; Nakagawa, K.; Fujino, S. Fabrication of fine α -alumina powders by thermal decomposition of ammonium aluminum carbonate hydroxide (AACH). *Acta Mater.* **2000**, *48*, 4735–4741. [CrossRef]
54. Wang, W.; Bi, J.; Qi, Y.; Zhang, Z.; Xing, Z.; Zhu, H.; Guo, D.; Xu, J.; Bai, Y. Preparation of micrometer-sized α-Al_2O_3 platelets by thermal decomposition of AACH. *Powder Technol.* **2010**, *201*, 273–276. [CrossRef]
55. Yong-Taeg, O.; Kim, S.; Shin, D. Fabrication and synthesis of α-alumina nanopowders by thermal decomposition of ammonium aluminum carbonate hydroxide (AACH). *Colloids Surf. A Physicochem. Eng. Asp.* **2008**, *314*, 415–418. [CrossRef]
56. Zhang, H.J.; Wang, X.J.; Jia, Q.L.; Sun, H.W. Artificial neural network analysis of preparation of nano α-Al_2O_3 powders by thermal decomposition of ammonium aluminium carbonate hydroxide. *Mater. Sci. Technol.* **2007**, *23*, 1021–1027. [CrossRef]
57. Huang, Y.; Xia, Y.; Liao, S.; Tong, Z.; Liu, G.; Li, Y.; Chen, Z. Synthesis of α-Al_2O_3 platelets and kinetics study for thermal decomposition of its precursor in molten salt. *Ceram. Int.* **2014**, *40*, 8071–8079. [CrossRef]
58. He, H.; Wang, Y.; Farkas, B.; Nagy, Z.K.; Molnar, K. Analysis and prediction of the diameter and orientation of AC electrospun nanofibers by response surface methodology. *Mater. Des.* **2020**, *194*, 108902. [CrossRef]
59. Tsekmes, I.A.; Kochetov, R.; Morshuis, P.H.F.; Smit, J.J. Thermal conductivity of polymeric composites: A review. In Proceedings of the 2013 IEEE International Conference on Solid Dielectrics (ICSD), Bologna, Italy, 30 June–4 July 2013; pp. 678–681. [CrossRef]
60. Hill, R.F.; Supancic, P.H. Thermal Conductivity of Platelet-Filled Polymer Composites. *J. Am. Ceram. Soc.* **2002**, *85*, 851–857. [CrossRef]